Three-Dimensional Failure Envelope of Concrete Dam Shear Keys

Mario Freitas[a], Mahdi Ben Ftima[a], Pierre Léger[a*], Najib Bouaanani[a]

[a]Department of Civil, Geological and Mining Engineering, Polytechnique Montréal, 2500 Chemin de Polytechnique, Montréal, QC H3C 3A7, Canada

* Corresponding author, email: pierre.leger@polymtl.ca

Abstract: Shear keys provide interlocking mechanisms along the vertical contraction joints of many concrete gravity dams. The shear key ultimate shear capacity is typically estimated as a function of the friction and cohesion that could be mobilised across a 2D shear plane located at the base of the key when subjected to a normal confinement pressure, P. A two-dimensional response of dam monoliths and shear keys shearing-off at their bases, is assumed. However, evidence of 3D interlocking behaviour between dam monoliths and the possibility of different key failure mechanisms involving interacting axial, P, shear, V, moment, M, and torsion, T, indicates that typical empirical formulations could significantly overestimate the actual shear key capacity under floods and seismic loadings. This paper presents an evaluation of the load–displacement response of shear keys subjected to multiaxial loading via nonlinear finite element analyses. A concrete "Continuous Surface Cap Model" (CSCM), available in the computer program LS-Dyna, is first shown to best capture the experimental shear keys' ultimate and residual shear capacity responses among five constitutive models. The effects of the tensile strength, fracture energy, confinement pressure, friction coefficient, initial opening, and dilation conditions on the load–displacement response of keys are investigated. Failure envelopes considering the key multiaxial shear capacity with confinement pressure, P, moment, M, and torsion, T, are developed. The ratios between moment and shear, M/V, and torsion and shear, T/V, control the failure mechanism. Increasing these ratios significantly reduce the ultimate shear capacity.

Keywords: Concrete gravity dams; Nonlinear FE Analysis; Shear keys; Multi-axial loading; Failure mechanisms; Failure Envelope

1. Introduction

Existing concrete gravity dams, built several years ago with shear keys along the vertical contraction joints (Figs. 1a, b), were most often initially designed using a bidimensional (2D) structural analysis, with minimal consideration for seismic loads. These dams are periodically reassessed to evaluate their structural stability while being subjected to anticipated extreme earthquake and flood loads according to the latest state-of-the-art and practice. The presence of shear keys provides some load transfer between monoliths, promoting three-dimensional (3D) interlocking upon sliding initiation and therefore increasing the structural strength that can be mobilised [1-7]. Ageing concrete dams in need of rehabilitation can therefore benefit from the additional resistance provided by existing shear keys, reducing the costs of potential retrofitting.

Including contraction joint shear keys in the structural analysis of concrete dams to assess the demand capacity ratios and related failure mechanisms can be carried out with different degrees of sophistication, using linear or nonlinear finite element (FE) analysis. Multiple empirical formulations have been developed to estimate the shear resistance of shear keys (Table 1). Many of these were developed in the context of concrete segmental bridges [8-13], and some were developed in the context of concrete dams [14]. These formulations estimate the shear resistance as a function of the frictional resistance and cohesion. The assumed failure mechanism is the shearing-off of the shear key at its base. However, shear keys can also fail by crushing the key edge and through dislocation mechanisms (Fig. 2a). In these cases, the shear strength may differ from that estimated from empirical formulations. In the shearing-off of the shear key base mechanism, first a single curvilinear crack is formed (S crack). Then, multiple diagonal cracks (M cracks) are formed along the base of the shear key, and the S crack increases in both length and width. Finally, the M cracks connect to one another, and the key base is sheared off, closing the S

crack at the same time (Fig. 2b). The magnitude of the confinement pressure also affects the cracking pattern, promoting greater variation in the failure mechanisms (Fig. 2c).

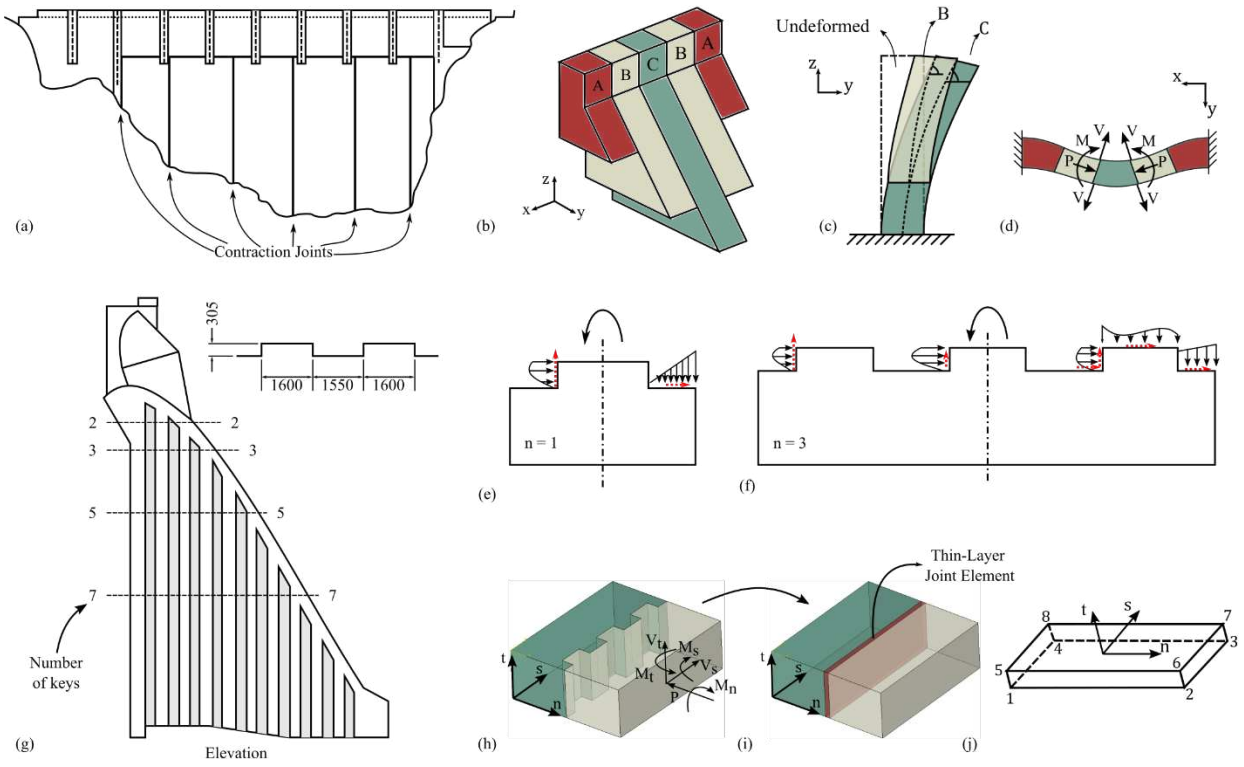

Figure 1 – Overview of the problem studied: (a) profile of a gravity dam, (b) simplified 3D model of a dam with blocks of different heights, (c) simplified deformed shape of dam blocks assuming no interlocking, (d) multiaxial loading on simplified dam contraction joints assuming interlocking, (e) contact forces on a single shear key submodel, (f) contact forces on a three-key submodel, (g) elevation section of a spillway with shear key, (h) detailed submodel of a keyed contraction joint, (i) submodel of a contraction joint with a thin-layer joint element, (j) thin layer joint element formulation.

If no interlocking is considered, taller dam monoliths deflect more under hydrostatic, flood, or seismic loads than shorter monoliths due to their stiffness differences (Fig. 1c). However, if interlocking is considered a torsional moment is developed along the joint. Moreover, interlocking generates bending moments due to differences in deflections along the cross-valley direction (Fig. 1d). The bending moment induces normal and tangential contact forces on the key, contributing to

Mode I (tensile) and Mode II (shear) failures (Figs. 1e, f). In sections with multiple shear keys, this contribution can lead to sequential (domino) failure of the shear keys [15]. The number of shear keys in a cross-section varies along the height of the dam (Fig. 1g). Both the shear resistance [10] and the bending and torsional stiffness [16] were demonstrated to vary nonlinearly with the number of shear keys in a section.

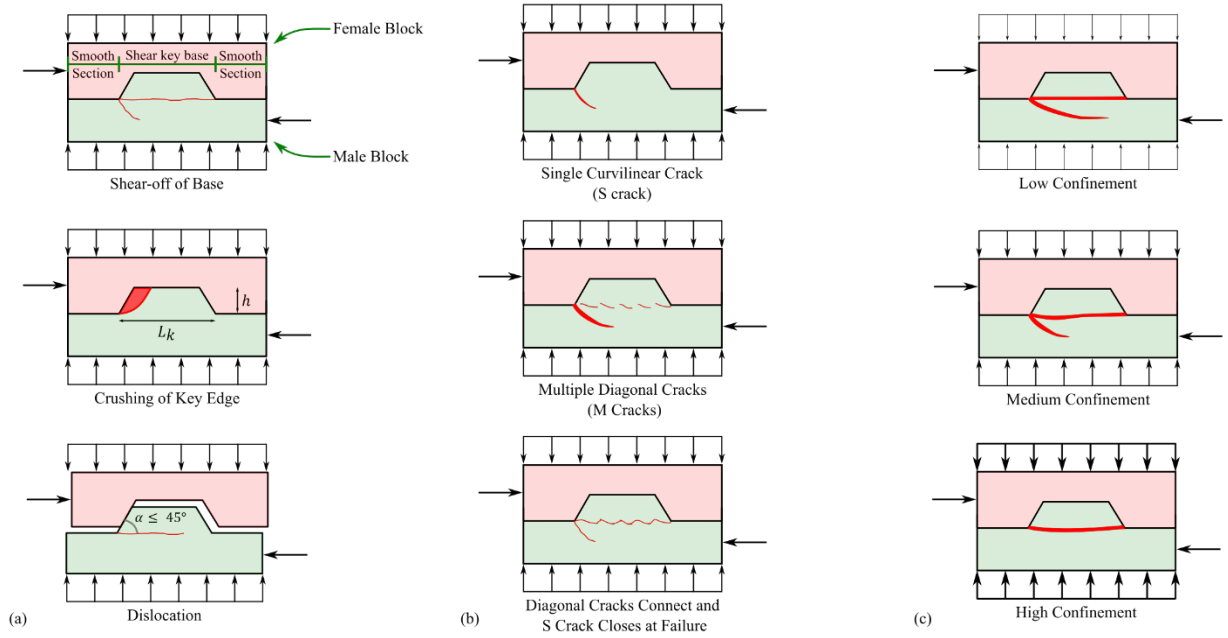

Figure 2 – Shear key failure mechanisms: (a) types of failure (adapted from [17]), (b) evolution of cracking on the shear-off of the base mechanism (adapted from [18]), (c) crack pattern for different confinement pressures (adapted from [19]).

Because the scale of shear keys is much smaller than the scale of the dam, modelling the detailed key geometry in nonlinear FE to accurately capture nonlinear behaviour requires unrealistically fine meshes. Thus, numerical models of dams often simplify shear keys in contraction joints as high-stiffness linear springs that prevent slipping of the joint, thus ignoring possible failure of the shear keys [20-23]. Another approach is to attribute a cohesive strength to the shear keys. If the shear stress at the joint exceeds the cohesive strength, then the key is assumed to fail, and the

residual strength is frictional only [15, 24-27]. Qiu et al. [28] proposed a method to simplify the geometry of actual shear keys, replacing them by a few large keys. Du et al. [29] used a similar approach, simplifying all the small trapezoidal shear keys in a joint by a large trapezoidal key. Zhang et al. [30] proposed a multiscale model where the shear keys are modelled with a fine mesh, the dam body is modelled with a coarse mesh, and a glue mesh is used to transition between the two. However, these models did not account for the reduction in the strength of shear keys due to accumulated damage, an initial opening of the shear keys, or interactions with bending and torsion. Ignoring the nonlinear response of shear keys may lead into underestimating the relative displacements of a structure under earthquake loads, especially under low peak ground acceleration that may be able to damage particularly weak keys [15, 31].

The current literature presents knowledge gaps concerning the nonlinear 3D modelling and simulation of dam contraction joints with shear keys, especially on the following topics: (i) residual strength of the damaged keys; (ii) key strength considering interacting axial, shear, bending and torsional loads; (iii) effect of imperfections and the initial opening of the contraction joint; (iv) effect of lateral boundary conditions allowing or preventing dilation while shearing is taking place; (v) effects of spatial variation of strength and stiffness of shear keys. Moreover, there is also a fundamental difference between the global dam response to floods or earthquake loads. Flood loads are applied as external water pressure restricted to the dam upstream face, while earthquake-induced inertial loads are distributed all over the dam body. Herein, nonlinear FE analyses of shear keys are performed to study some of these topics. The focus is put on the response of single key specimens, loaded externally at the local level in accordance with typical experimental set-up found in the literature. First, an appropriate concrete constitutive model is selected and calibrated. Then, an appropriate range of values for the material parameters is defined. An analysis of two

104 dam monoliths, subjected to external upstream face pressure, with a contraction joint modelled
105 with detailed shear keys is performed to study the global behaviour of the contraction joints.
106 Subsequently, a submodel with one rectangular shear key is used for parametric analyses of the
107 material parameters, boundary, contact, and initial conditions. Finally, failure envelopes for the
108 interactions between the confinement pressure, shear, and moment (P-M-V) and between the
109 confinement pressure, shear, and torsion (P-T-V) are developed. This work serves as a basis for
110 understanding the detailed nonlinear behaviour of shear keys. Future studies in this research
111 project will study shear keys of different shapes and sections with multiple keys. Once the
112 behaviour of contraction joints submitted to 3D loading is clearly understood at the shear key level
113 (Fig. 1h), a thin-layer joint element (Fig. 1j) with an equivalent response will be developed to
114 substitute the detailed modelling of the shear keys (Fig. 1i) and applied to contraction joints of
115 gravity dams modelled numerically.

116 Table 1 - Formulations for the shear capacity of shear keys.

Author	**Formulation**
Buyukozturk et al. [11]	$V_j = A_j\left(0.65\sqrt{f_c'} + 1.36\sigma_n\right)$
AASHTO [8]	$V_j = A_k\sqrt{f_{ck}}(0.2048\ \sigma_n + 0.9961) + 0.6\ A_{sm}\sigma_n$
Romabch and Specker [12]	$V_j = 0.14 f_c' A_k + 0.65\sigma_n A_j$
Turmo et al. [13]	$V_j = A_k \frac{\sqrt[3]{f_{ck}^2}}{100}(7\sigma_n + 33) + 0.6A_{sm}\sigma_n \quad \text{if} f_{ck} \leq 50\ \text{MPa}$
Curtis and Lum [14]	$V_k = \left(0.464 f_c'^{\frac{2}{3}} + \sigma_n \tan\phi\right) A_k$
Alcalde et al. [10]	$V_j = 7.118\ A_k(1 - 0.064\ N_k) + 2.436\ A_{sm}\sigma_n\ (1 + 0.127\ N_k)$
Ahmed and Aziz [9]	$V_j = 0.6\sigma_n A_{sm} + (1.06A_k + 2100\sigma_n)\sqrt{f_c'}$

Note: V_j is the shear resistance of the joint (including the key sections and smooth sections), V_k is the shear resistance of the key (not including the smooth sections) A_j is the total area of joint surface, A_k is the area of the base of the shear key, $A_{sm} = A_j - A_k$ is the area of smooth surfaces of the joint, f_c' is the uniaxial concrete compressive strength, f_{ck} is the concrete characteristic strength, σ_n is the confinement pressure, ϕ is the concrete friction angle, and N_k is the number of keys in the joint.

2. Selecting the Concrete Constitutive Model

Appropriately selecting a concrete constitutive model that can capture both the shear key peak shear capacity and its post-peak behaviour is essential for a reliable dam safety assessment under flood and earthquake loads. With this objective in mind, five concrete constitutive models were examined in a preliminary study: (i) *Concrete Damage Plasticity* (CDP/ABAQUS) [32], (ii) "*Endommagement Progressif Multiaxial Tridimensionnel*" (user-defined subroutine – EPM3D/ABAQUS) [33], (iii) *Karagozian & Case Concrete* (KCC/LS-Dyna) [34], (iv) *Continuous Surface Cap Model* (CSCM/LS-Dyna) [35], and (v) *StahlBETonAnalyse* (SBETA/ATENA) [36]. Among these models, the CSCM was found to best capture the post-peak behaviour of shear keys reported in experimental data from the literature, as shown later in section 2.4. Moreover, the CSCM could be efficiently calibrated to closely fit the experimental data and match the reported peak shear capacity.

In the following section, a brief description of the theoretical formulation of the CSCM is provided. Then, the procedure used to calibrate the CSCM is presented. A comparison between the experimental results and the five constitutive models studied is presented. The adopted selection procedure for the fracture energy of mass concrete, an important parameter to model the key post-peak behaviour, is also discussed.

2.1 Description of the CSCM

The CSCM is a constitutive model initially designed to predict the dynamic response of concrete roadside safety structures subjected to collisions with motor vehicles. Despite being developed for roadside safety applications, this constitutive model has also been applied to many other static and dynamic structural concrete problems [37-40]. The CSCM is an elastoplastic damage model, with a smooth and continuous intersection between the shear failure surface and a hardening cap to simulate a plastic volume change as a function of the hardening rule described herein later. The cap can expand and contract to determine the shape of the pressure-volumetric strain curves. The

initial location of the cap determines the beginning of plastic behaviour in uniaxial compression [41]. This constitutive model presents (i) isotropic behaviour, (ii) a three stress-invariant shear surface with translation for pre-peak hardening, (iii) damage-based softening with an option for the erosion of elements, and (iv) strain rate effects (Fig. 3).

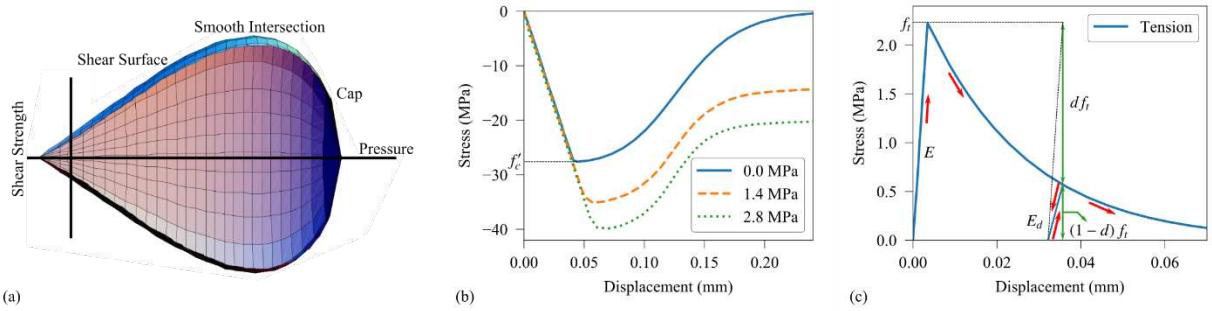

Figure 3 – The CSCM: (a) failure surface, (b) compressive behaviour for confinement pressures of 0.0 MPa, 1.4 MPa and 2.8 MPa, (c) tensile behaviour (adapted from [35]).

The theoretical formulation of the CSCM is described in [35] and briefly reviewed herein. The yield function f is defined as a function of the stress invariants J_1, J_2', and J_3', and the cap hardening parameter κ (Eq. 1).

$$f(J_1, J_2', J_3', \kappa) = J_2' - \Re^2 F_f^2 F_c \tag{1}$$

where F_f is the shear failure surface, F_c is the hardening cap, and $\Re$ is the Rubin three-invariant reduction factor. $\Re$ is a scaling function that changes the radius and shape of the yield surface in the deviatoric plane to account for the fact that concrete fails at lower values of J_2' in triaxial extension and torsion than in triaxial compression. For example, this shape can be a circle, as in the Drucker–Prager and von Mises models, a hexagon, as in the Mohr–Coulomb model, or an irregular hexagon, as in the William-Warnke model. The shear failure surface F_f is a function of

160 J_1, and the model parameters α, β, λ, and θ are used to fit the CSCM to triaxial compression tests
161 (Eq. 2).

$$F_f(J_1) = \alpha - \lambda \exp(-\beta J_1) + \theta J_1 \tag{2}$$

162 The hardening cap F_c is a function of J_1 and κ (Eq. 3).

$$F_c(J_1, \kappa) = \begin{cases} 1 - \dfrac{(J_1 - \kappa)^2}{(X - \kappa)^2}, & J_1 \geq \kappa \\ 1, & otherwise \end{cases} \tag{3}$$

163 where X and κ control the contraction and expansion of the cap, simulating the plastic volume
164 change. The intersection between the shear surface and the cap is at $J_1 = \kappa$, and X is defined as

$$X(\kappa) = L(\kappa) + RF_f\big(L(\kappa)\big) \tag{4}$$

165 where $L(\kappa)$ is the maximum of the calculated value of κ and its initial value κ_0, and a model input
166 parameter R is another model input parameter representing the ellipticity ratio of the cap. The
167 contraction and expansion of the cap are based on the hardening rule (Eq. 5).

$$\varepsilon_v^p = W(1 - \exp(-D_1(X - X_0) - D_2(X - X_0)^2)) \tag{5}$$

168 where ε_v^p is the plastic volume strain, W is the maximum plastic volume strain, X_0 is the initial
169 location of the cap when $\kappa = \kappa_0$, and D_1 and D_2 are model input parameters.

170 The CSCM can be used with minimal input parameters, providing only the compressive strength,
171 f_c', and maximum aggregate size, d_a. In this case, an initialization routine determines the
172 remaining material properties, such as the bulk modulus, Poisson's ratio, fracture energy, and
173 strain rate parameters. The initialization routine was calibrated for concrete with a compressive
174 strength between 28 MPa and 58 MPa [35].

When used with minimal input, the CSCM assumes a Poisson's ratio $\nu = 0.15$ that is independent of the concrete strength. The modulus of elasticity E is given by [42]:

$$E = E_C \left(\frac{f_c'}{10}\right)^{1/3} \quad (6)$$

where f_c' is the compressive strength in MPa and $E_c = 18{,}275$ MPa. The model parameters α, β, λ, and θ, used to relate the concrete strength to pressure in triaxial compression, as well as their equivalents for torsion and triaxial extension, are calibrated from experimental data on plain concrete cylinders and fitted with a quadratic equation. Likewise, the uniaxial tensile strength f_t is related to the compressive strength f_c' using the quadratic relationship:

$$f_t = -0.0018 f_c'^2 + 0.185 f_c' - 1.58 \; (for \; 28 \leq f_c' \leq 58) \quad (7)$$

The uniaxial tensile strength is not a direct input material parameter in the CSCM. Instead, the concrete strength must be adjusted following Eq. 7 to meet a target uniaxial tensile strength. The fracture energy G_F is obtained as:

$$G_F = G_{F0} \left(\frac{f_c'}{10}\right)^{0.7} \quad (8)$$

where G_{F0} is the fracture energy at $f_c' = 10$ MPa, provided experimentally in [42]. However, these values of the fracture energy are not adequate for mass concrete, as shown herein later. The default values of G_F are initially used in the calibration process (using structural concrete), but are replaced with more appropriate values when studying concrete dam shear keys (using mass concrete).

Damage in the CSCM is defined as a function of the ratio between the damaged (E_d) and undamaged modulus of elasticity (E) (Fig. 3c). Thus, it varies from 0 to 1 and is calculated as:

$$d = 1 - \frac{E_d}{E} \tag{9}$$

2.2 Modelling of the Shear Key Concrete-Concrete Interface

The contact between the male and female blocks of the shear key is modelled using an automatic surface-to-surface algorithm. This is a two-way contact algorithm, meaning that the nodes on both the master and slave surfaces are checked for penetration. The penetrations are treated with a contact formulation where penetrating nodes are pushed back in the normal direction with force F_n (Eq. 10).

$$F_n = kD_p \tag{10}$$

$$k = \frac{f_s \cdot A_s^2 \cdot \overline{K}}{V} \tag{11}$$

where k is the stiffness of the contact, D_p is the penetration depth, f_s is the penalty factor, A_s is the area of the contact segment, $\overline{K}$ is the bulk modulus of the contacted element and V is the volume of the contact element. The penalty factor f_s is set to its default value of 1.0, and no significant interpenetration is observed in the simulations with these settings.

In the tangential direction, a frictional force F_f (Eq. 12) is applied to the contacting surface.

$$F_f = \mu F_n \tag{12}$$

where μ is the static friction coefficient. Additionally, the option to switch from node-to-segment formulation to segment-to-segment formulation (SOFT=2) is activated, as recommended for this type of contact [43].

205 **2.3 Calibration of the CSCM**

206 The CSCM presents five interesting features:

207 • It can be used with a minimal input, where only the compressive strength and aggregate
208 size are required as the input parameters.
209 • The material parameters, which are generated automatically when using minimal input, can
210 be recovered and modified by the user if needed be. A second run of the analysis with user-
211 defined parameters can be performed, allowing for efficient calibration.
212 • The load–displacement response obtained with the CSCM captures the post-peak strength
213 reduction and the residual capacity observed in experimental data from the literature as
214 demonstrated herein later.
215 • The model has the option to erode (delete) highly damaged and distorted elements, a feature
216 that generally improves the numerical stability in the finite element simulations.
217 • The CSCM can be used with an explicit solver with robust convergence properties for
218 nonlinear contact problems and is suitable for dynamic applications. This is relevant for
219 future stages of this project, where shear keys under cyclic and dynamic loads will be
220 studied.

221 Experimental data on the failure of trapezoidal shear keys from Jiang et al. [44] are used for the
222 calibration of the CSCM, while experimental data from Zhou et al. [45] are used only for the
223 validation of the model. Jiang et al. [44] tested a shear key that is 100 mm wide, 35 mm deep, and
224 100 mm thick (Fig. 4c), and Zhou et al. [45] tested a shear key that is 100 mm wide, 50 mm deep,
225 and 250 mm thick (Fig. 4a). They also tested specimens with 3 shear keys, where each key is 100
226 mm wide, 50 mm deep, and spaced 50 mm apart from one another (Fig. 4b). Both authors [44, 45]
227 use a 12 mm rebar to prevent premature cracking outside of the region of the shear keys and tested

multiple specimens with varying concrete strengths, confinement pressures, and numbers of shear keys. The specimens used for the performance assessment (and calibration) of CSCM are presented in Table 2.

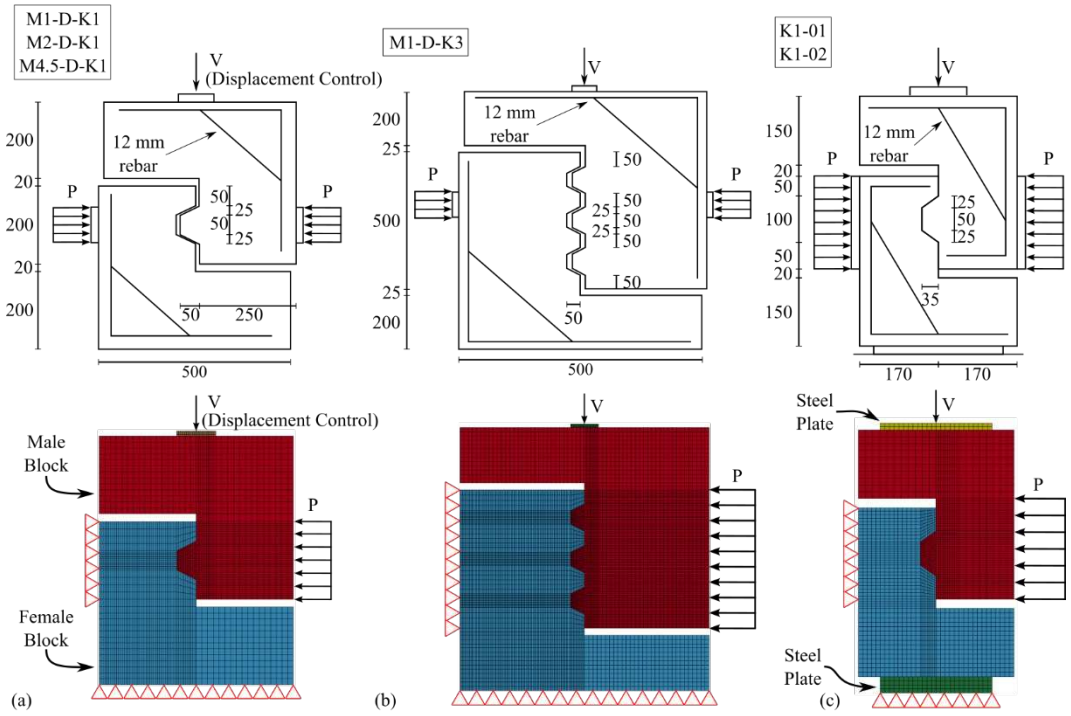

Figure 4 – Shear key models used for the performance assessment (dimensions in mm) – experimental tests and numerical models: (a) M1-D-K1, M2-D-K1 and M4.5-D-K1, (b) M1-D-K3, (c) K1-01, K1-02.

The finite element models built to replicate these experiments (Fig. 4) are 3D models with a single finite element in the thickness direction. The concrete blocks are modelled with the CSCM using minimal input with the same concrete strength as the experimental tests (Table 2) and d_a equal to 19 mm. The steel support plates are modelled using a linear elastic material with a modulus of elasticity of 200 GPa and a Poisson's coefficient of 0.3. The reinforcing steel bars (rebars) are modelled as elastoplastic truss elements embedded in the concrete elements. The rebars are fully bonded to concrete elements. No relative sliding between rebars and concrete is permitted. For the

boundary conditions, the bottom support plate is fixed in the vertical direction, the side of the female block is fixed in the horizontal direction, and the back face of the entire model is fixed in the out-of-plane direction. Poisson's effect is not restricted in the out-of-plane direction. The confinement pressure is then applied on the male side of the key. The shearing load is applied as an imposed displacement of the middle nodes of the top support plate (Fig. 4).

Table 2 – Experimental tests on the shear keys

Author	Specimen Name	f_c' (MPa)	Confining Stress (MPa)	Number of Keys	Shear Capacity (kN)
Jiang et al. [44]	K1-01	41.5	1.0	1	89.7
	K1-02	41.5	2.0	1	113.9
Zhou et al. [45]	M1-D-K1	38.7	1.0	1	193.0
	M2-D-K1	56.2	2.0	1	335.0
	M4.5-D-K1	37.1	4.5	1	375.0
	M1-D-K3	35.7	1.0	3	446.0

The CSCM requires a total of 46 parameters. Thus, choosing each parameter individually is very challenging. To perform the calibration, a minimal input model with concrete compressive strength, f_c', and maximum aggregate size, d_a,was first used to recover the 46 model parameters. The resulting *"default"* normalized shear stress-displacement responses overestimate the peak strength by an average of 17% (Fig. 5). The peak response is also generally overestimated and, in some cases, presents a brittle behaviour (Figs. 5a, b). To improve the correlation between the predictions and the experimental results, the following four main parameters were modified one at a time: (i) the flag enabling cap retraction (IRETRC), which controls the shape of the load–displacement response but also reduces the bearing capacity; (ii) the aspect ratio of the cap surface (R), which controls the displacement at ultimate capacity; (iii) the maximum plastic volume compaction (W), which controls the shear capacity; and (iv) the parameter controlling element

erosion (ERODE), which affects the stability of the numerical solution. These parameters were chosen because they most significantly affect the computed load–displacement responses.

Specimens K1-01 and K1-02 (Table 2) are used for the calibration. Parameter optimization is performed using LS-OPT [46], which is an optimization tool that interfaces with LS-Dyna [47]. The load–displacement curves obtained from the numerical models are fitted against the experimental curves through a curve mapping algorithm. The flag IRETRC is set to a discrete sampling with values of 0 or 1. The aspect ratio R is set to a starting value of 5, a minimum of 1, and a maximum of 10. The variable W is set to a starting value of 0.05 with a minimum of 0.01 and a maximum of 0.2. The ERODE parameter is set to a starting value of 1.1 with a minimum of 1.0 (to erode an element when d in Eq. 9 reaches 0.99) and a maximum of 1.1 (to erode an element, d has to reach 0.99 and a strain of 10%). The random point selection for each of those parameters is performed with the D-optimal algorithm [48]. The simulations are performed taking 16 points for each parameter for 3 iterations, reducing the domain at each iteration. After performing this optimization, the parameters that best fit the experimental curves are $R = 9.023$, $W = 0.105$, $ERODE = 1.067$, and cap retraction activated.

The responses for the calibrated CSCM and default CSCM (using minimal input) are compared against the experimental data from [44, 45] (Fig. 5). The structural responses are presented in the normalized shear stress-displacement curves. The normalized shear stress ($\tau/\sqrt{f_c'}$) is the ratio between the shear stress at the base of the shear key and the square root of the concrete strength. The shear stress at the base of the shear key is considered to be uniform and equal to the total shear force (vertical force) applied divided by the area of the base of the key. The displacement in the response curves refers to the imposed displacement at the top support plate. Compared to the experimental results by Zhou et al. [45], the calibrated model overestimates the peak shear capacity

283 by an average of 6%, as opposed to 19% for the default parameters. The calibrated post-peak
284 response is also similar to the experimental response, both in terms of the shape of the softening
285 branch and in the residual capacity value. The calibrated model yields a good agreement with the
286 experimental results for models with one and three shear keys. For high confinement pressures,
287 the calibrated model yields a good estimate of the shear capacity but underestimates the residual
288 capacity, while the default model overestimates the shear capacity but provides a good estimate of
289 the residual capacity (Fig. 5e).

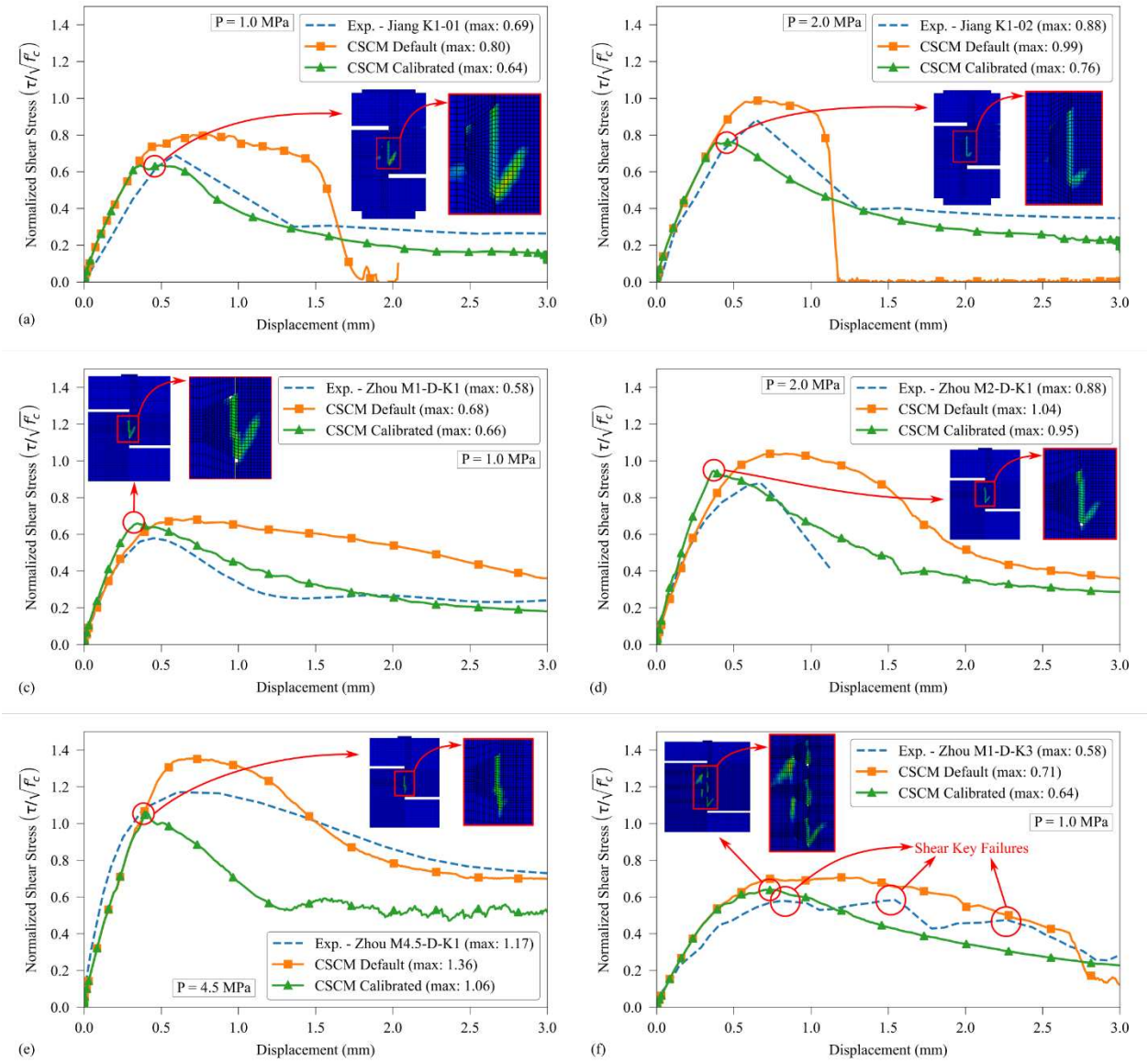

Figure 5 – Validation of CSCM against experimental data: (a) K1-01, (b) K1-02, (c) M1-D-K1, (d) M2-D-K1, (e) M4.5-D-K1, (f) M1-D-K3.

2.4 Comparison with Other Constitutive Models

The results obtained with the calibrated CSCM were compared with other constitutive models for specimen K1-01 (Table 2, Fig. 6). The other constitutive models were also calibrated according to their peak strength, and the results presented are the best attempts for each model. KCC yielded

298 the best results with its default parameters. CDP is calibrated using linear softening in tension and
299 the Hognestad model in compression, as well as the recommended model parameters [32]. EMP3D
300 is calibrated with the recommended failure surface and material parameters [33]. SBETA is
301 calibrated with exponential tension softening, a rotated crack model, and default parameters [36].
302 The CSCM is the model that best captures the ultimate shear capacity (~7% difference from
303 experimental values), the displacement at peak response, and the post-peak softening. Other
304 models, except for CDP, provided good estimates of the ultimate shear capacity. However, all
305 other models had a very brittle post-peak response, which was not observed experimentally [44,
306 45]. Differences in response obtained from each constitutive model as compared to experimental
307 results are expected because of a number of factors, including, among others: (i) different mode I
308 continuum cracking formulation (isotropic in CDP, CSCM and KCC, anisotropic in SBETA and
309 EPM3D), (ii) different concrete shear damage formulations, (iii) different solution algorithms
310 (implicit in ATENA, explicit in ABAQUS and LS-Dyna), (iv) different handling of severely
311 damaged elements (with options of erosion in CSCM and EPM3D, but not in others). Hence the
312 importance of evaluating and validating each constitutive model.

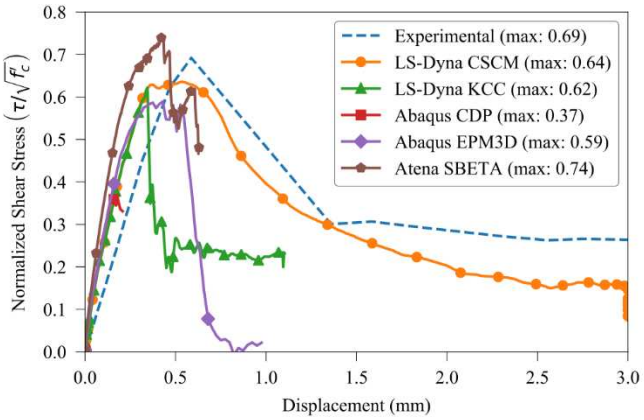

313

Figure 6 – Comparison of the shear response of shear key K1-01 [44] using different constitutive models.

2.5 Fracture Energy for Mass Concrete Models

The fracture energy is a material parameter commonly used to model the tensile softening of concrete. It can be characterised by the parameter G_F, which accounts for the total energy in the cracking process, or G_f, which accounts for the energy relative to the initial portion of the softening curve. The maximum load supported by a structure is controlled by G_f, while the post-peak behaviour is more dependent on G_F [49].

Several authors developed different empirical equations to estimate the values of G_f and G_F using a combination of the following parameters: compressive strength f_c', tensile strength f_t, maximum aggregate size d_a, water-cement ratio w/c, and parameters for the shape of the aggregate α_0 and γ_0 (Table 3).

It is also important to distinguish between the experimentally measured fracture energy and the asymptotic fracture energy $G_{F\infty}$. For a given concrete mix, the ratio h_2/d_a between the concrete ligament length, h_2, and maximum aggregate size, d_a, controls the fracture energy measured experimentally. Most wedge splitting experimental setups use a ratio of $h_2/d_a = 3$. However, a ratio of $h_2/d_a = 10$ is required to obtain fracture energy values within 10% of $G_{F\infty}$ [50]. In a dam block, a crack propagating within the bulk material could have the potential to approach $G_{F\infty}$. On the other hand, a crack that propagates at the base of a shear key could be limited to the size of the key, reflecting values of G_F that are more akin to lower h_2/d_a ratios.

A set of 30 experimental specimens with large aggregate sizes (typically present in concrete dams) tested for fracture energy was tabulated from the literature (Table A.1). These data were used to

test the accuracy of the empirical equations to estimate G_F in Table 3. It is found that the equation proposed by Guan et al. [51] gives an upper bound estimate of the fracture energy, while the modified equation by Bazant and Becq-Giraudon [52] yields a lower bound estimate. This reflects the fact that Guan et al. [51] derives their equations from wedge splitting tests with $h_2/d_a > 6$ while Bazant and Becq-Giraudon [52] derives their equations from wedge splitting tests with $h_2/d_a = 3$.

Table 3 – Fracture Energy Equations

Author	Equation
Bazant and Oh [53][1]	$\begin{cases} G_f = (2.72 + 0.0214 f_t') f_t'^2 \left(\frac{d_a}{E}\right) \\ c_f = 1.811 + 0.0143 f_t' \end{cases}$
Wittman et al. [54]	$G_F = 0.97 f_c' + 41.8$
CEB-FIP [42]	$G_F = (0.0469 d_a^2 - 0.5 d_a + 26)\left(\frac{f_c'}{10}\right)^{0.7}$
CEB-FIP [56] – Structural Concrete	$G_F = 73 f_{cm}^{0.18}$ $f_{cm} = f_{ck} + \Delta f$ $\Delta f = 8\ MPa$
Kim et al. [57]	$G_F = 1041\left(1 - e^{-0.07 f_c'}\right)$ $L_{ch} = 4.94(\mathrm{f_c'})^{-0.87}$
Bazant and Becq-Giraudon [52][2]	$G_F = 2.5 G_f$ $G_f = \alpha_0 \left(\frac{f_c'}{0.051}\right)^{0.46} \left(1 + \frac{d_a}{11.27}\right)^{0.22} \left(\frac{w}{c}\right)^{-0.30}$ $c_f = \exp\left[\gamma_0 \left(\frac{f_c'}{0.022}\right)^{-0.019} \left(1 + \frac{d_a}{15.05}\right)^{0.72} \left(\frac{w}{c}\right)^{0.2}\right]$
Bazant and Becq-Giraudon [52] – Modified[3]	$G_F = 2.5\alpha_0 \left(\frac{f_c'}{0.062}\right)^{0.43} \left(1 + \frac{d_a}{3.95}\right)^{0.97} \left(\frac{w}{c}\right)^{-0.2}$
Beygi et al. [58] - Self Compacting Concrete	$G_F = 37.3 f_c'^{0.29}$ $G_f = 5.39 f_c'^{0.516}$ $L_{ch} = 2.253 f_c'^{-0.49}$
Beygi et al. [59] – Self Compacting Concrete	$G_F = 37.2 d_a^{0.401} \left(\frac{f_c'}{10}\right)^{0.107}$ $G_f = 9.26 d_a^{0.31} \left(\frac{f_c'}{10}\right)^{0.42}$
Guan et al. [51]	$G_F = (0.1616 d_a + 1.0263) f_c'$

[1]The value of G_F is estimated as$G_F = 2.5 G_f$
[2] For rounded aggregates, $\alpha_0 = \gamma_0 = 1$ and for crushed or angular aggregates $\alpha_0 = 1.44$ and $\gamma_0 = 1.12$.
[3]The modified version was obtained by redoing the statistical analysis by Bazant and Becq with a restricted dataset to obtain an equation that is more fit to mass concrete.

3. Global behaviour of monolith joints with multiple keys

An analysis of a 78 m dam model with 3 monoliths was performed to study the global behaviour of the shear keys and the effects of dilation. Given the large scale of the model, a coarse mesh is used. Therefore, the local behaviour of shear keys is not captured accurately, hence the need of

local analyses using a submodel presented hereafter. The middle monolith is subjected to a uniform load to shear the keys, and each dam monolith is 15 m wide. However, a symmetry boundary condition is used, and only one and a half monoliths are used (Fig. 7a). The dam is modelled under both free and restrained dilation conditions. Under restrained dilation, the lateral displacement of the side face of both monoliths is restricted, while under free dilation, only the half-width monolith has the lateral displacement restricted to impose the symmetry condition. For both models, the damage patterns and displacements of the keys and monoliths are studied at a mid-height cross-section (at an elevation of 39 m). When dilation is not restrained, the upstream shear keys are sheared at their base (Fig. 7b). In addition, the joint tends to open downstream. When the dilation is restrained, the joint remains closed, and the damage level at this cross-section is much smaller (Fig. 7c). This shows that the shear key load bearing capacity is dependent on the boundary conditions of the monoliths. Moreover, the opening of the joints observed when dilation is permitted introduces a bending moment in the joint that interacts with the shear load and reduces the ultimate capacity of the keys.

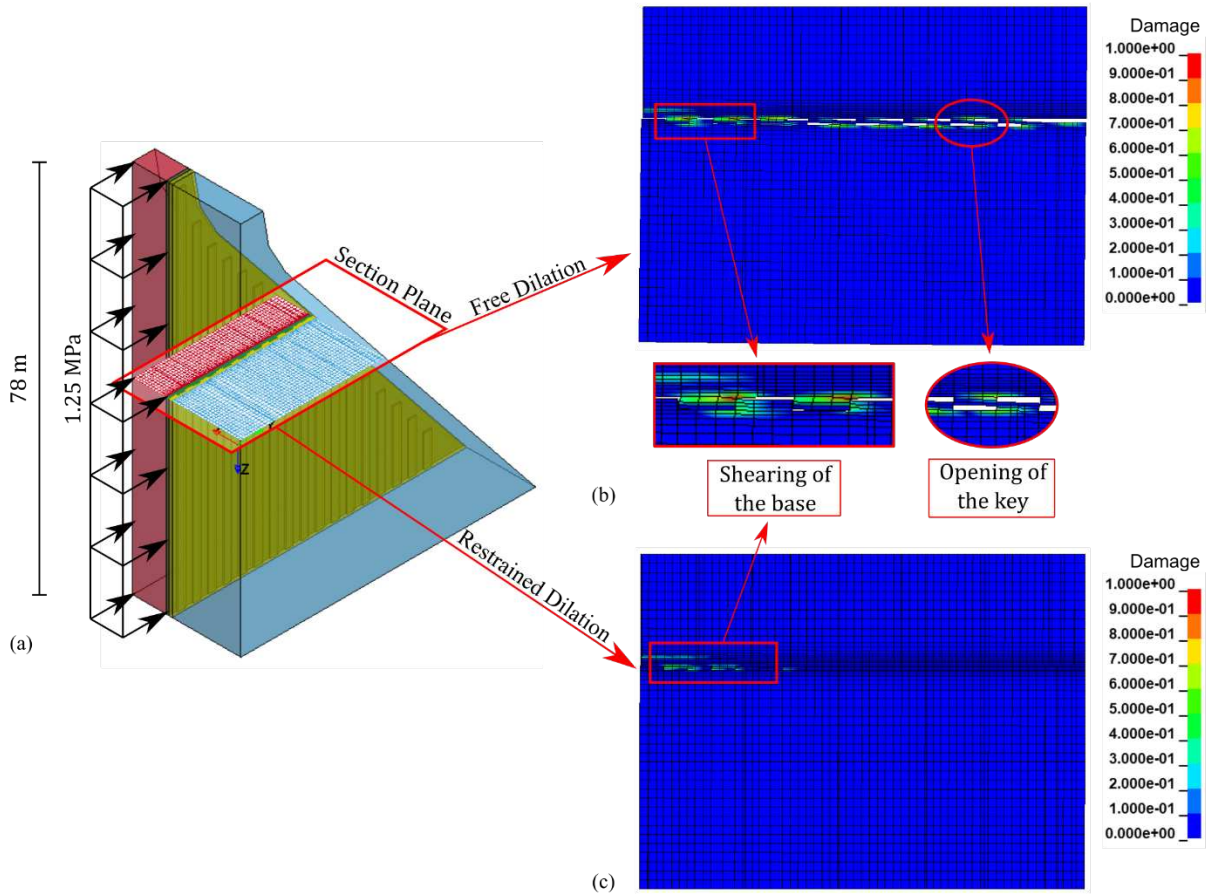

Figure 7 – Two monoliths with shear keys: (a) the finite element model, (b) damage and opening of shear keys under free dilation, (c) damage of shear keys under restrained dilation.

4. Parametric Analysis of a Rectangular Shear Key

A parametric analysis of rectangular shear keys is performed to assess the influence of (i) material parameters, (ii) contact parameters, (iii) lateral boundary conditions, and (iv) initial opening on the shear capacity and load–displacement responses. The analyses are performed on contraction joint submodels containing a single shear key. The submodels (geometry and material parameters) are based on an existing 58 m concrete gravity dam with $f_c' = 29$ MPa and a maximum aggregate size of 150 mm [60]. By default, the compressive strength f_c' is set to 29 MPa, the fracture energy G_F is set to 250 N/m, the friction coefficient μ is set to 1.0, and the confinement pressure P is set to 1.0 MPa, allowing for free dilation. In the parametric analyses, only one parameter is modified at

a time. Unless explicitly mentioned, the remaining parameters use their default values. The shear key studied is 1.6 m wide and 0.3 m deep (Fig. 8a). The models used to study the interaction between torsional and shear loads are 8 m thick to allow for better distribution of torsion (Fig. 8c). The numerical models use the calibrated CSCM presented herein for concrete near the shear keys. Outside of the region where damage is expected, an elastic constitutive model is used (Fig. 8). The confinement pressure P and bending moment M are applied as pressure loads on the side of the shear key block, the torsion T is applied as a pressure load in the middle section of the shear key, and the shearing load V is applied through an imposed displacement of the top nodes of the male shear key block.

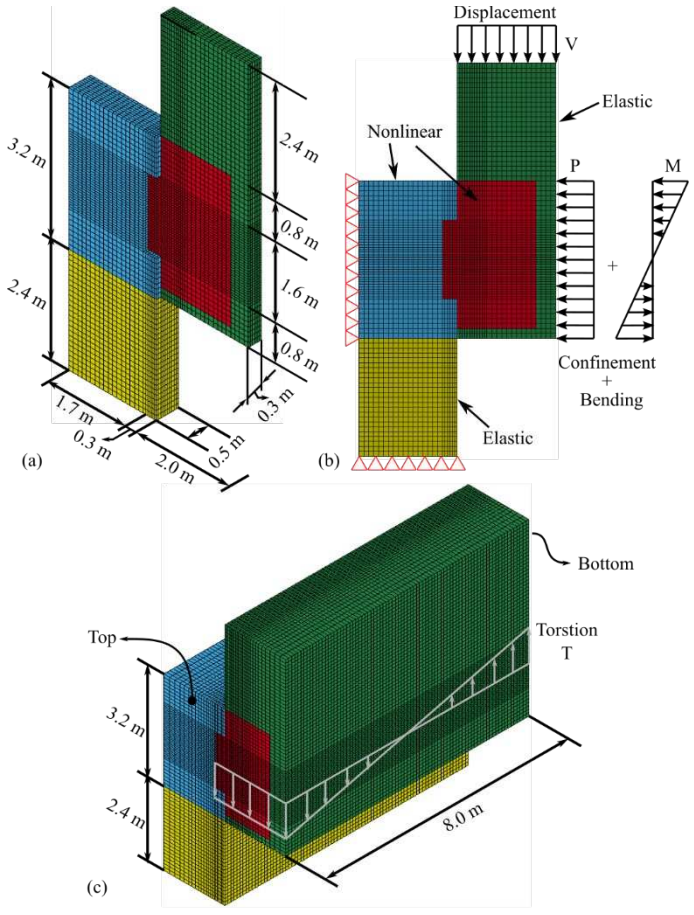

Figure 8 – Finite element models used for the parametric analysis: (a) default model geometry, (b) boundary conditions, (c) torsional model geometry

4.1 Tensile Strength and Fracture Energy

The strength of concrete dam shear keys is usually estimated as a function of the joint's friction and cohesion, following the Mohr–Coulomb criterion. The frictional force developed on the joint is the product of the normal load and the concrete-concrete friction coefficient. The cohesion can be estimated as twice the direct tensile strength based on Griffith's failure criterion [61]. Accordingly, Curtis and Lum [14] provided an estimate of the shear strength of dam shear keys (Table 1). Hereafter, a parametric analysis of the shear keys is conducted considering uniaxial tensile strengths of the bulk material of 1.42 MPa, 1.97 MPa, 2.29 MPa, 2.96 MPa, and 3.16 MPa. These values correspond to compressive strengths f_c' of 20 MPa, 25 MPa, 29 MPa, 40 MPa, and 50 MPa, respectively (Eq. 7). With $f_t = 1.42$ MPa, the shear key reaches an ultimate normalised shear stress of 0.52, and then the base of the key is sheared off. For higher concrete strengths, the failure mechanism observed is the formation of a diagonal crack followed by crushing of the key edge. (Fig. 9a), where the higher the tensile strength is, the higher the ultimate normalised shear stress and the longer the diagonal crack observed at the peak response.

The second material parameter studied was the fracture energy G_F, with values of 100 N/m, 250 N/m, 400 N/m, 550 N/m, and 700 N/m. The fracture energy does not affect the ultimate shear capacity; however, the higher G_F is, the higher the post-peak residual shear capacity is, and less damage that is observed at the peak response (Fig. 9b).

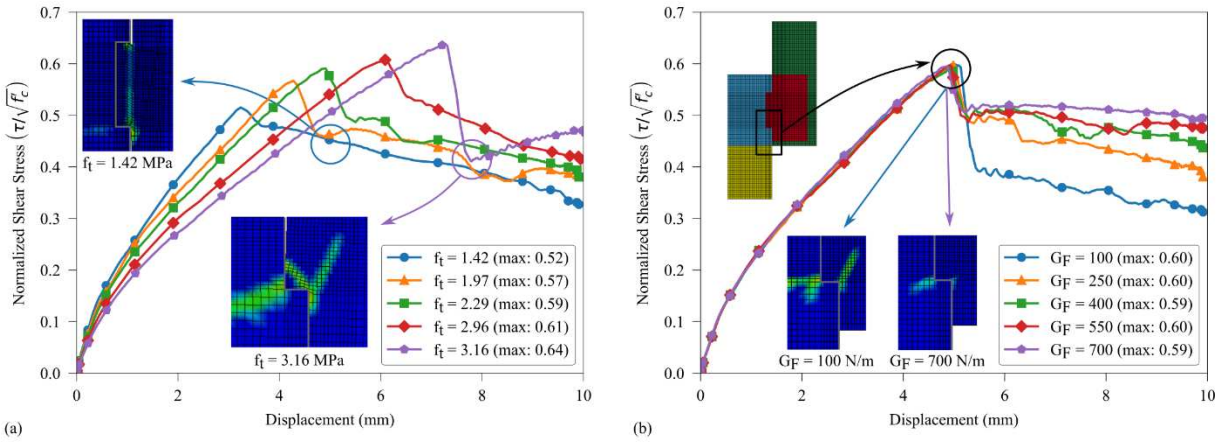

Figure 9 – Parametric variation of the material properties: (a) tensile strength f_t, (b) fracture energy G_F.

4.2 Confinement Pressure and Friction Coefficient

The contact forces transferred between the male and female blocks depend on the confinement pressure P and the friction coefficient μ. The grouting of the contraction joints, if applicable, and the seasonal temperature variations introduce confinement pressure on the contraction joints. Under normal circumstances, the dam monoliths are presumed to be interlocked and in contact with one another. Thus, when the keys are being sheared, the effect of dilation is restrained by the adjacent dam blocks. However, if there is an initial opening or if the contraction joints open during an earthquake, then the shear keys may be free to dilate. Herein, the restrained dilation condition is achieved by restricting the lateral movement of the nodes on the side of the male key block after applying the confinement pressure.

In this section, a parametric variation of the confinement pressure P and friction coefficient μ is performed for cases with free and restrained dilation. Under a condition of no confinement pressure ($P = 0$ MPa) and free dilation, an ultimate normalised shear stress of 0.3 is obtained irrespective of the value of the friction coefficient μ. This is because no frictional force is developed on the

contraction joint in the shearing direction. Because of the free dilation condition, the male block moves away from the female block, and a diagonal crack is formed from the edge of the key (Fig. 10a).

When dilation is restrained, an additional confinement pressure is applied to the contraction joint as the key is sheared. Therefore, more frictional force is developed along the contact interface, and the ultimate shear capacity increases. The restrained dilation condition also changes the failure mechanism for $P = 0.0$ MPa. A diagonal crack is initially developed, but the ultimate shear capacity is reached immediately before the lower-left edge of the male shear key is crushed under compression (Fig. 10a). This failure mechanism is also observed for $P = 1.0$ MPa and $P = 2.0$ MPa whether dilation is permitted or restrained (Figs. 10b, c). The additional confinement pressure introduced by restraining dilation is also observed for $P = 1.0$ MPa and $P = 2.0\ MPa$.

Higher confinement pressure increases the ultimate shear capacity as well as the residual capacity. It also reduces the length of the diagonal crack formed before reaching the peak response, especially under the free dilation condition (Fig. 10b, c). Increasing the friction coefficient increases the ultimate shear capacity for any condition other than $P = 0.0$ with free dilation (Fig. 11a). It also changes the path, angle, and length of the diagonal crack. The larger the friction coefficient is, the smaller and more vertical the diagonal crack. Fig. 11b shows the crack patterns developed for $P = 1.0$ MPa with free dilation. Similar behaviour is observed for $P = 1.0$ MPa with restrained dilation, as well as $P = 0.0$ MPa and $P = 2.0$ MPa with both free and restrained dilation.

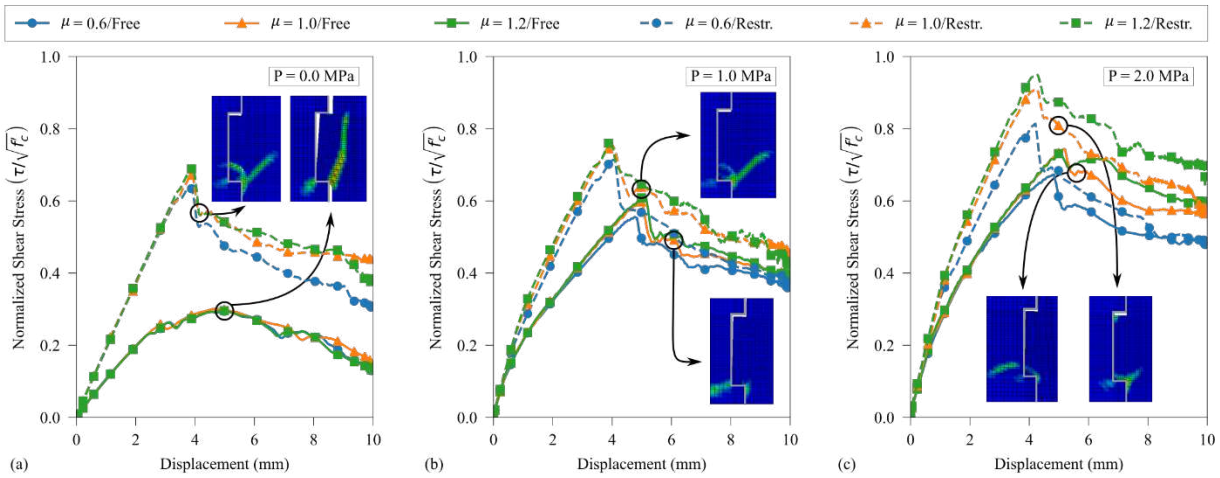

441

442 Figure 10 – Parametric analysis of the confinement pressure and friction coefficient: (a) P = 0.0
443 MPa, (b) P = 1.0 MPa, (c) P = 2.0 MPa
444

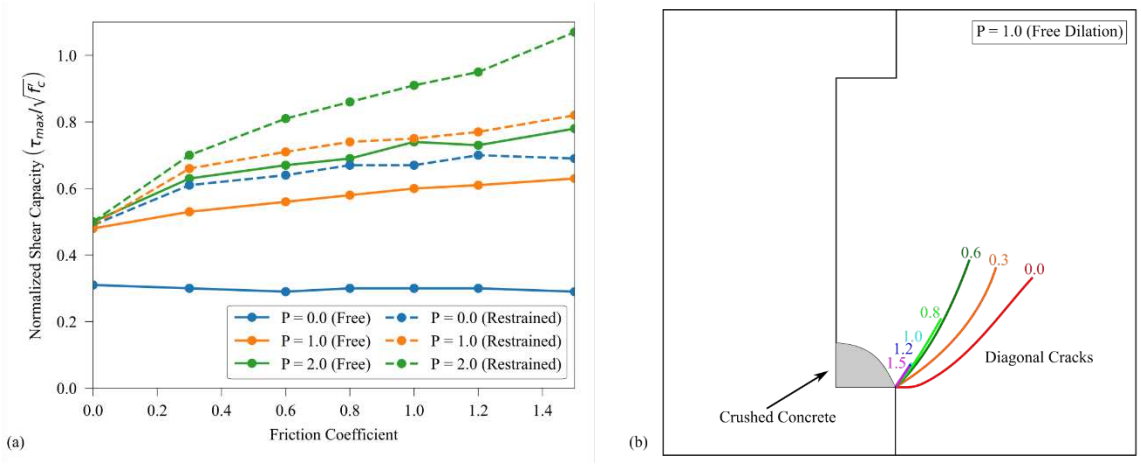

445

446 Figure 11 – Interaction P-V-μ: (a) normalised shear capacity response, (b) diagonal crack path
447 for P = 1.0 MPa and μ from 0.0 to 1.5.
448

449 The empirical formulations for estimating the shear key capacity presented in Table 1 generally
450 assume a friction coefficient of 0.6 for structural concrete. Then, a comparison between the
451 analytical results and the numerical predictions with $\mu = 0.6$ (free dilation and restrained dilation)
452 is presented in Table 4. The Buyukozturk et al. [11], AASHTO [8], Alcalde et al. [10], and Curtis
453 and Lum [14] formulations better match the restrained dilation cases. The AASHTO [8]

formulation provides the best performance for restrained dilation, underestimating the shear capacity by an average of 10% compared with the numerical results. Ahmed and Aziz [9], Rombach and Specker [12], and Turmo et al. [13] better match the free dilation cases. The Rombach and Specker [12] formulation provides the best performance for free dilation, overestimating the shear capacity by 4% on average. The Curtis and Lum [14] formulation, with $\mu = 0.6$, is typically used for shear keys in dams, but it overestimates the shear capacity by 28% in restrained dilation and by 100% in free dilation for this particular key configuration.

Table 4 – Comparison of the shear stress capacity between the numerical and analytical results.

Confinement Pressure	0.0 MPa	1.0 MPa	2.0 MPa
Numerical (CSCM)/Free Dilation	1.56 MPa	3.02 MPa	3.61 MPa
Numerical (CSCM)/Restrained Dilation	3.44 MPa	3.83 MPa	4.36 MPa
Buyukozturk et al. [11]	3.50 MPa (2.24/1.02)	4.86 MPa (1.61/1.27)	6.22 MPa (1.72/1.43)
AASHTO [8]	2.68 MPa (1.72/0.78)	3.53 MPa (1.17/0.92)	4.38 MPa (1.21/1.01)
Rombach and Specker [12]	2.03 MPa (1.30/0.59)	2.68 MPa (0.89/0.70)	3.33 MPa (0.92/0.76)
Turmo et al. [13]	1.56 MPa (1.00/0.45)	2.19 MPa (0.72/0.57)	2.82 MPa (0.78/0.65)
Alcalde et al. [10]	3.33 MPa (2.14/0.97)	4.70 MPa (1.56/1.23)	6.08 MPa (1.68/1.39)
Curtis and Lum [14]*	4.38 MPa (2.81/1.27)	4.98 MPa (1.65/1.30)	5.58 MPa (1.55/1.28)
Ahmed and Aziz [9]	2.85 MPa (1.83/0.83)	3.17 MPa (1.05/0.83)	3.48 MPa (0.96/0.80)

Note: Values in the parenthesis are ratios between the empirical estimation and the numerical results obtained with free dilation and with restrained dilation, respectively.

* Using $\tan(\phi) = 0.6$

4.3 Initial Opening and Imperfections

A shear key initial opening may be caused by imperfections in the moulding of keys during construction or the sequential grouting process, seasonal temperature variations, or pre-existing damage to the dam. A parametric analysis including the variation of the initial openings of 0%, 10%, 20%, 50%, and 75% of the depth of the key (30 cm) is performed. The case with a 0% initial

opening is equivalent to the case with a confinement pressure of $P = 0.0$ MPa. Increasing the initial opening reduces the ultimate shear capacity but does not modify the failure mechanism. In fact, in this parametric analysis the failure mechanism is dependent on the dilation condition (Fig. 12).

An initial opening of 10% reduces the shear capacity by 7% for the case with free dilation. However, when dilation is restrained, the shear capacity is reduced by 39% (Fig. 13). This difference in behaviour can be explained as follows. If the joint is initially closed, a restrained dilation induces an additional confinement pressure on the contraction joint, thus increasing the shear capacity. However, if the joint is initially open, then the dilation does not affect the confinement pressure on the joint. Nevertheless, the ultimate shear capacity considering a small initial opening and restrained dilation is still larger than when considering free dilation because of the different failure mechanisms (Fig. 13).

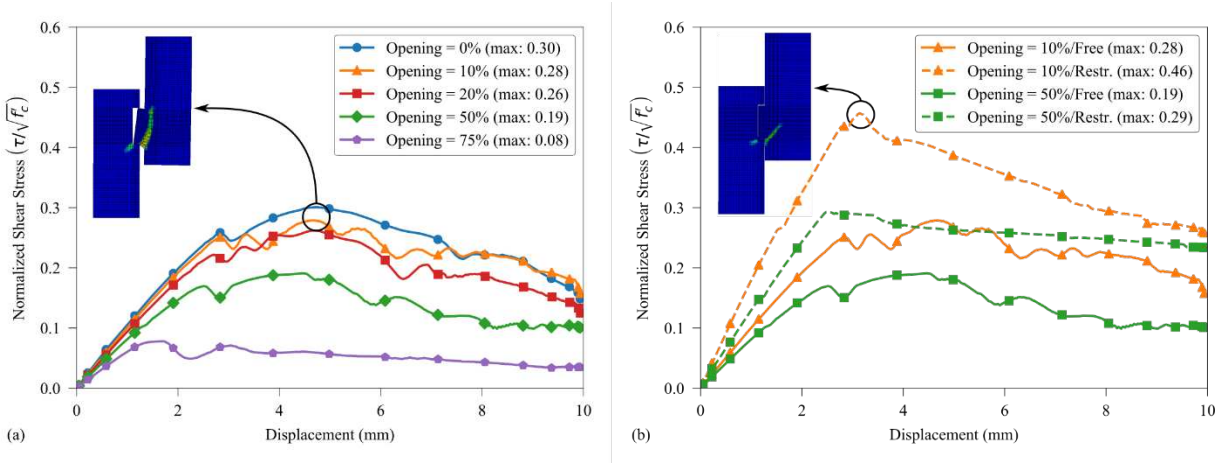

Figure 12 – Parametric analysis of the initial opening: (a) free dilation, (b) free and restrained dilation.

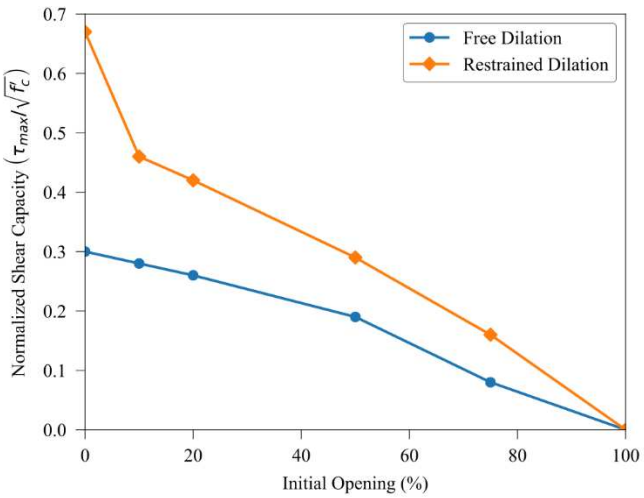

Figure 13 – Interaction between the initial opening and normalised shear capacity.

5. Multiaxial Failure Envelope for a Rectangular Shear Key

The 3D nature of stresses in dam contraction joints (Fig. 1) and the possible opening of the contraction joints (Fig. 7) show that shear keys could be subjected to a significant bending moment and torsion. In this section, we study the interactions between the confinement pressure, bending moment and shear (P-M-V), as well as the interactions between confinement pressure, torsion, and shear (P-T-V) and how it affects the shear key load carrying capacity.

5.1 Confinement Pressure and Bending Moment

The interaction between the bending moment and shear is studied by applying the confinement pressure first and then simultaneously applying the shear and bending moment. Shear is introduced as an imposed displacement, and the bending moment is introduced as a triangular pressure load (Fig. 8b). The load combinations are labelled P*x*-V*yy*-M*zz*, where *x* is the input confinement pressure in MPa, *yy* is the target imposed displacement in mm, and *zz* is the target bending moment in MN.m. The normalised shear stress-displacement response is obtained for varying ratios of the applied bending moment and shear (Fig. 14). All load cases are considered with free dilation. Only

positive bending moment cases are presented because these are the most critical cases. The applied shear causes compression at the bottom edge of the key, while on the other hand a negative bending moment relieves the compression at the bottom edge of the key, increasing the load capacity. Thus, having no bending moment is a more critical case than having a negative bending moment.

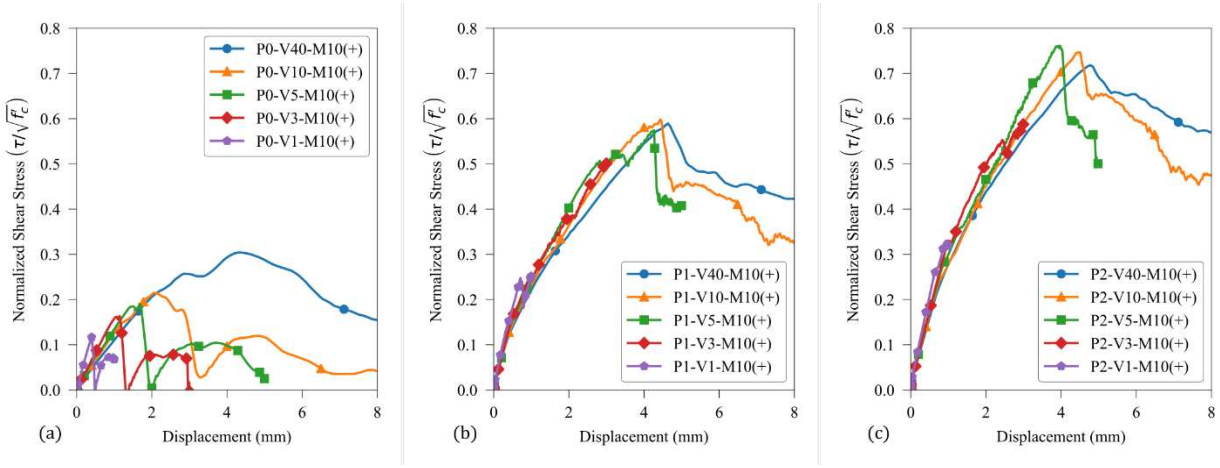

Figure 14 – Parametric analysis of confinement pressure (P), shear (V) and bending moment (M): (a) P = 0.0 MPa, (b) P = 1.0 MPa, (c) P = 2.0 MPa.

The combinations of the bending moment and shear that are applied to the key at a peak response are plotted in Fig. 15. The shear is measured in MN per m of thickness of the male block, and the bending moment is measured in MN.m per m of thickness. The applied shear is then calculated by subtracting the vertical load imposed by the bending moment only at the point of peak response from the total vertical load. The applied bending moment is then calculated by recovering the input bending moment at the point of peak response. The interaction between the bending moment and shear follows a bilinear behaviour for $P = 1.0$ MPa and $P = 2.0$ MPa. For a ratio of the applied moment divided by the applied shear $M/V > 0.7$, the observed failure mechanism is an unstable propagation of the diagonal crack, where the crack propagates in a brittle manner all the way to the boundary of the model when a certain damage threshold is exceeded (Fig. 15d). For $M/V <$

0.7, the observed failure mechanism is crushing of the shear key edge (Fig. 15b). For $M/V \cong 0.7$; both mechanisms are observed almost simultaneously (Fig. 15c). The change in the failure mechanism from crushing of the shear key edge to unstable propagation of the diagonal crack significantly reduces the ultimate shear capacity (Figs. 14, 15a).

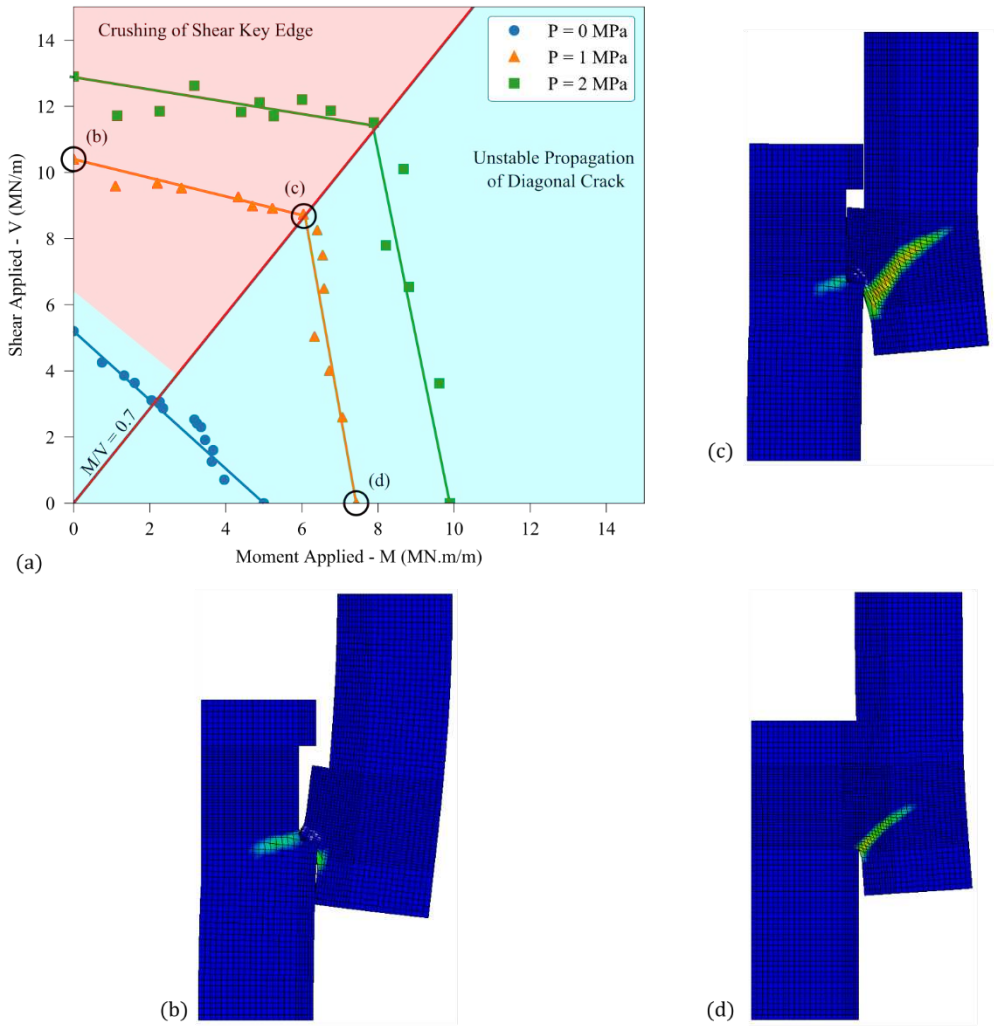

Figure 15 – Interaction between the confinement pressure, shear, and bending moment: (a) P-V-M failure envelope, (b) crushing of the edge failure mechanism, (c) mixed failure mechanism, (d) unstable propagation of diagonal crack failure mechanism (displacements are magnified by 100 times in deformed shapes).

For $P = 0.0$ MPa, only the unstable propagation of the diagonal crack failure mechanism is observed. This is consistent with the results obtained for $P = 0.0$ MPa without a bending moment and with free dilation. Because the case without a bending moment also fails by unstable propagation of a diagonal crack, applying the bending moment does not affect the failure mechanism. However, the bending moment reduces the ultimate shear capacity in a nearly linear manner (Fig. 15a).

5.2 Confinement Pressure and Torsional Moment

The interaction between torsion and shear is studied using the same methodology applied for the interaction with the bending moment. Only positive torsion is presented because the results are symmetrical for negative torsion. The P-V-T interaction is nonlinear (Fig. 16a). For $P = 1.0$ MPa and $P = 2.0$ MPa, with a ratio of torsion to shear $T/V < 27$, the shear key fails by crushing of the key edge at the top, immediately followed by shearing-off of the base at the bottom (Fig. 16b). For $P = 0.0$ MPa, a diagonal crack is formed, and the base of the key is sheared from the top to the bottom section (Fig. 16c). However, for $P = 1.0$ MPa and $P = 2.0$ MPa, with $T/V > 27$ the shear key fails in tension due to the significant concentrated load at the middle section where the torsion is applied (Fig. 16d). This type of failure is a consequence of the boundary condition used to introduce torsion; the actual shear capacity in those cases might be higher.

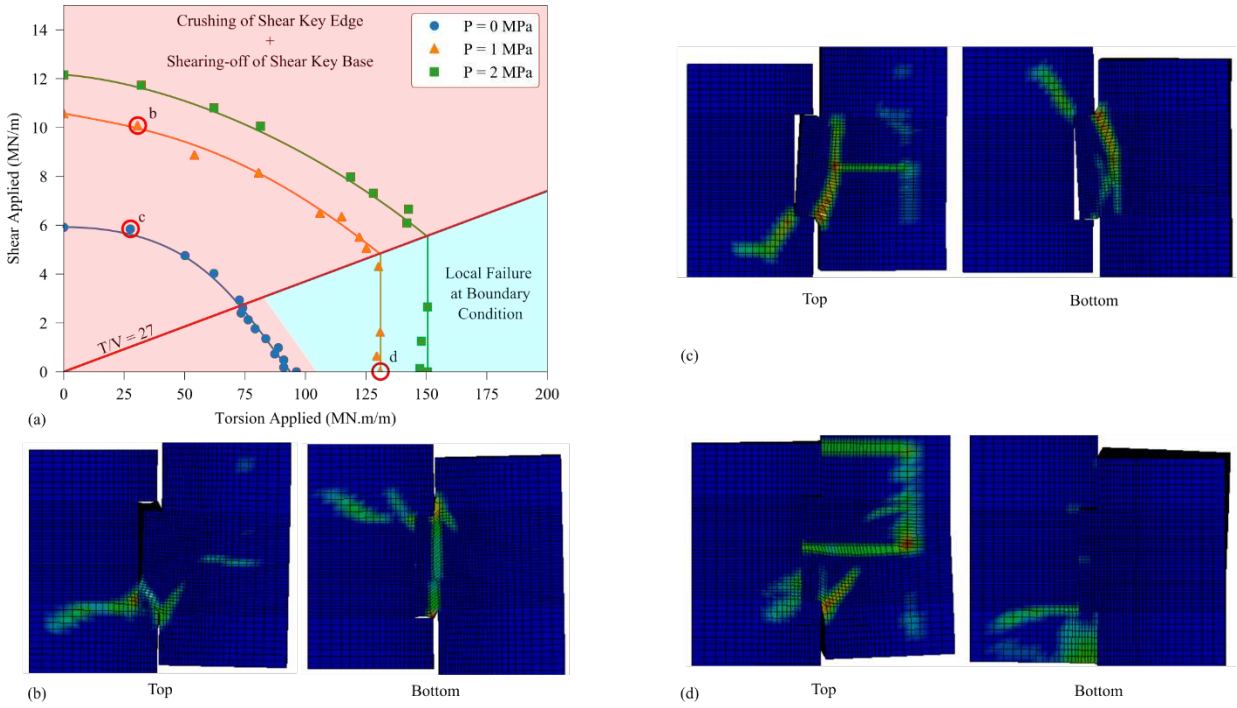

Figure 16 –Interaction between the confinement pressure, shear, and torsion: (a) P-V-T failure envelope, (b) crushing of the key edged at the top and shearing of the base at the bottom, (c) shearing of the base for $P = 0$ MPa, (d) local failure on the plane of application of torsion.

6. Conclusions

The failure mechanism and related shear strength of shear keys along contraction joints in concrete dams has been traditionally estimated using a one-dimensional failure mechanism with empirical formulas. However, 3D multiaxial loading conditions reduce the shear strength that could be mobilized. The objective of this study was to quantify the peak and residual strength of shear keys considering multiaxial loading interactions. A numerical model using the LS-Dyna Continuous Surface Cap Model (CSCM) was calibrated against experimental data available in the literature and adapted to study concrete dam shear keys. A preliminary analysis of two adjacent gravity dam monoliths (78 m high) with shear keys in the contraction joints showed that the upstream shear keys fail by shearing of the base, while the opening of the keys increases downstream at a 39 m

559 high section. A submodel with a single shear key based on an existing 58 m gravity dam was
560 modelled to study the influences of the material parameters, boundary conditions, initial opening,
561 and the interactions between the normal forces, bending moment, torsion, and shear on the load–
562 displacement response and failure mechanism of shear keys.

563 The following conclusions are drawn from the case studies presented:

564 • From a comparison among five concrete constitutive models, it was determined that the
565 CSCM provided the most satisfactory agreement with the experimental load–displacement
566 response of concrete shear keys, especially at the post-peak range.
567 • In a dam section with multiple shear keys, the openings of the keys, due to an external
568 pressure applied at the upstream face, increase from upstream to downstream when the
569 keys are free to dilate. This indicates that shear keys are subjected to a bending moment
570 that affects the failure load and failure mechanism of the keys.
571 • An increase in the concrete tensile strength from 1.42 MPa to 3.16 MPa causes an increase
572 in the normalised shear capacity ($\tau/\sqrt{f'c}$) of the keys from 0.52 to 0.64 and the maximum
573 displacement of the key at a peak load from 3.24 mm to 7.32 mm.
574 • An extensive study was done to determine the upper bound and lower bound of fracture
575 energy. An increase in the fracture energy from 250 N/m to 700 N/m causes an increase in
576 the post-peak shear capacity of approximately 15%. The ultimate shear capacity and
577 displacement at failure are not significantly modified by an increase in the fracture energy.
578 • The dilation condition of the shear key greatly influences its shear capacity. Restrained
579 boundary dilation of the shear key increases its shear capacity by an average of 133% for
580 a confinement pressure of $P = 0$ MPa, compared to a free dilation condition.

- The shear capacity estimated using the analytical formulation by Curtis and Lum [14] (using $\tan(\phi) = 0.6$) overestimates the numerical results by 28% considering restrained dilation, and 80% considering free dilation.
- With free dilation, for $P = 2.0$ MPa, increasing the friction coefficient at the joint from $\mu = 0.0$ ($\phi = 0°$) to $\mu = 1.5$ ($\phi = 56°$) reduces the length of the diagonal crack, increases the crack angle, and increases the normalised shear capacity from 0.5 to 0.78. When considering restrained dilation, the increase in normalised shear capacity goes from 0.5 (for $\mu = 0.0$) to 1.07 (for $\mu = 1.5$).
- An initial joint opening of 20% of the shear key depth decreases the shear capacity by 14% with free dilation and 45% with restrained dilation. The case with restrained dilation presents a much greater reduction in shear capacity because the initial opening prevents the increase in confinement pressure due to dilation that would otherwise contribute towards a higher shear capacity.
- For the rectangular shear key model studied, when simultaneously applying a bending moment and shear, two different failure mechanisms are possible: (i) a diagonal crack propagates from the edge of the shear key into the bulk material for $M/V > 0.7$ (ratio between the bending moment and shear), or (ii) the shear key fails by crushing the edge of the shear key for $M/V < 0.7$. The failure envelope for $P = 1.0$ MPa and $P = 2.0$ MPa presents a bilinear diagram where the intersection between the two lines is approximately at $M/V = 0.7$. For $P = 0.0$ MPa, the only the diagonal crack mechanism is observed and the failure envelope is linear.
- Three failure mechanisms were observed in the parametric analyses: (i) shearing-off of the key base for low values of the concrete strength ($f_c' \leq 20$ MPa), (ii) crushing of the key

edge for $P > 0$ MPa and for $P = 0$ with a restrained dilation, and (iii) unstable propagation of a diagonal crack for $P = 0$ with free dilation and for ratios of $M/V > 0.7$.

The conclusions above were obtained for rectangular shear key submodels subjected to quasi-static monotonic loads. Moreover, the lateral boundary conditions are either free or completely restrained. The other boundary conditions are a simplification of the actual conditions in a complete dam. Future research will focus on a study of multiple shear keys of different geometries, the possibility of sequential failure, and the extension to cyclic and earthquake loadings.

CRediT authorship contribution statement

M. Freitas: Investigation, Visualization, Validation, Writing – Original Draft. **M. Ben Ftima:** Conceptualization, Writing – Review & Editing. **P. Léger:** Conceptualization, Methodology, Supervision, Writing – Review & Editing, Funding Acquisition. **Najib Bouaanani:** Supervision, Writing – Review & Editing.

Declaration of Competing Interest

The authors declare that they have no known competing financial interests or personal relationships that could have appeared to influence the work reported in this paper.

Acknowledgements

The financial support provided by the Natural Science and Engineering Research Council of Canada (NSERC) and the Fonds de Recherche du Québec – Nature et Technologies (FRQNT) is acknowledged. The support from Compute Canada and Calcul Québec is also acknowledged.

References

[1] Dowdell DJ, Fan BH. Practical Aspects of Engineering Seismic Dam Safety – Case Study of a Concrete Gravity Dam. 13th World Conference on Earthquake Engineering. Vancouver, B.C., Canada2004.

[2] Chopra AK. Earthquake Engineering for Concrete Dams. Hoboken, NJ: Wiley; 2020.

[3] Azmi M, Paultre P. Three-dimensional analysis of concrete dams including contraction joint non-linearity. Engineering Structures. 2002;24:757-71.

[4] Wang G, Wang Y, Lu W, Yu M, Wang C. Deterministic 3D seismic damage analysis of Guandi concrete gravity dam: A case study. Engineering Structures. 2017;148:263-76.

[5] NZSOLD. New Zealand Dam Safety Guidelines. 2015.

[6] Wang H, Feng M, Yang H. Seismic nonlinear analyses of a concrete gravity dam with 3D full dam model. Bulletin of Earthquake Engineering. 2012;10:1959-77.

[7] Guerra A. Shear Key Research Project Literature Review and Finite Element Analysis. Denver, Colorado: USBR; 2007.

[8] AASHTO. Guide Specifications for Design and Construction of Segmental Concrete Bridges. American Association of State Highway and Transportation Officials; 1999.

[9] Ahmed GH, Aziz OQ. Shear strength of joints in precast posttensioned segmental bridges during 1959–2019, review and analysis. Structures. 2019;20:527-42.

[10] Alcalde M, Cifuentes H, Medina F. Shear Strength of Dry Keyed Joints and Comparison with Different Formulations. VIII International Conference on Fracture Mechanics of Concrete and Concrete Structures. Toledo, Spain2013. p. 1-7.

[11] Buyukozturk O, Bakhoum MM, Beattie SM. Shear Behavior of Joints in Precast Concrete Segmental Bridges. Journal of Structural Engineering. 1990;116:3380-401.

[12] Rombach G, Specker A. Design of Joints in Segmental Hollow Box Girder Bridges. 1st FIB Congress. Osaka, Japan2002.

[13] Turmo J, Ramos G, Aparicio AC. Shear strength of match cast dry joints of precast concrete segmental bridges: proposal for Eurocode 2. Materiales de Construcción. 2006;56:42-52.

[14] Curtis DD, Lum K, K.Y. Estimated Strength of Shear Keys in Concrete Dams. CDA 2008 Annual Conference. Winnipeg, MB, Canada2008. p. 17-28.

[15] Amos P, Black J, Dungar R, Walker J. Utilising the Curved Footprint of an 80 Year Old Gravity Dam to Aid Performance During Extreme Earthquakes. 34th Annual USSD Conference. San Francisco, California2014. p. 177-94.

[16] Ben Ftima M, Lafrance S, Léger P. 3D Modelling of Shear Keys in Concrete Gravity Dams Using an Advanced Grillage Methodology. Water Science and Engineering. 2020;13:223-32.

[17] Lacombe G, Pommeret M. Les Joints Structuraux dans les Constructions en Grands Panneaux Prefabriques. Annales de ITBTP, Gros-Oeuvre No 18. Paris, France1974.

[18] Kaneko Y, Triantafillou TC, Leung CK. Fracture Mechanics Approach for Failure of Concrete Shear Key. I: Theory. Journal of Engineering Mechanics. 1993;119:681-700.

[19] Shamass R, Zhou X, Alfano G. Finite-Element Analysis of Shear-Off Failure of Keyed Dry Joints in Precast Concrete Segmental Bridges. Journal of Bridge Engineering. 2015;20.

[20] Løkke A, Chopra AK. Direct-Finite-Element Method for Nonlinear Earthquake Analysis of Concrete Dams Including Dam–Water–Foundation Rock Interaction. Berkeley, California: Pacific Earthquake Engineering Research Center; 2019.

[21] Chuhan Z, Jianwen P, Jinting W. Influence of seismic input mechanisms and radiation damping on arch dam response. Soil Dynamics and Earthquake Engineering. 2009;29:1282-93.

[22] Jiang S, Du C, Yuan J. Effects of shear keys on nonlinear seismic responses of an arch-gravity dam. Science China Technological Sciences. 2011;54:18-27.

[23] Toyoda Y, Shiojiri H, Ueda M, Tsunekawa K. Dynamic Analysis of an Existing Arch Dam Including Joint Non-Linearity and Dam-Waterfoundation Rock Interaction. 13th World Conference on Earthquake Engineering. Vancouver, BC2004.

[24] Lau DT, Noruziaan B, Razaqpur AG. Modelling of Contraction Joint and Shear Sliding Effects on Earthquake Response of Arch Dams. Earthquake Engineering and Structural Dynamics. 1998;27:1013-29.

[25] Gunn RM. The Design of Shear Keys for Large Arch Dams in Seismic Regions. 73rd Annual Meeting of ICOLD. Tehran, Iran2005.

[26] Ghiasian M, Ahmadi MT. Efficient 3D boundary element dynamic analysis of discontinuities. Engineering Analysis with Boundary Elements. 2015;50:320-8.

[27] Ahmadi MT, Izadinia M, Bachmann H. A discrete crack joint model for nonlinear dynamic analysis of concrete arch dam. Computer & Structures. 2001;79:403-20.

[28] Qiu Y-X, Wang J-T, Jin A-Y, Xu Y-J, Zhang C-H. Simple models for simulating shear key arrangement in nonlinear seismic analysis of arch dams. Soil Dynamics and Earthquake Engineering. 2021;151.

[29] Du C, Jiang S, Jiangsu N. Nonlinear Dynamic Responses of Arch Dam with Shear Keys. Mathematical and Computational Applications. 2010;15:828-33.

[30] Zhang L, Zhang H, Hu S. Failure Patterns of Shear Keys and Seismic Resistance of a Gravity Dam with Longitudinal Joints. Journal of Earthquake and Tsunami. 2014;08.

[31] Wei B, Li C, Jia X, He X, Yang, M. Effects of shear keys on seismic performance of an isolation system. Smart Structures and Systems. 24;3:345-360.

[32] Dassault Systèmes. Abaqus 6.14 - Abaqus/CAE User's Guide. Providence, Rhode Island2014.

[33] Massicote B, Ben Ftima M. EPM3D-v3 - A User-Supplied Constitutive Model for the Nonlinear Finite Element Analysis of Concrete Structures. Montreal: École Polytechnique de Montréal; 2017.

[34] Malvar LJ, Crawford JE, Wesevich JW, Simons D. A Plasticity Concrete Material Model for DYNA3D. International Journal of Impact Engineering. 1997;19:847-73.

[35] Murray YD. Users Manual for LS-DYNA Concrete Material Model 159. U.S. Department of Transportation; 2007.

[36] Cervenka Consulting. ATENA Program Documentation - User's Manual for Atena 2D. Prague, Czech Republic2015.

[37] Wu Y, Crawford JE, Magallanes JM. Performance of LS-DYNA Concrete Constitutive Models. 12th International LS-DYNA® Users Conference. Detroit, Michigan2012.

[38] Bohara RP, Tanapornraweekit G, Tangtermsirikul S. Investigation of concrete material models for analysis of seismic behavior of reinforced concrete under reversed cyclic load. Songklanakarin J Sci Technol. 2019;41.

[39] Coleman DK. Evaluation of Concrete Modeling in LS-DYNA for Seismic Application [Master's Thesis]. Austin, Texas: University of Texas at Austin; 2016.

[40] USBR. Evaluation of Nonlinear Material Models in concrete Dam Finite Element Analysis. Dam safety Technology Development Program. Denver, Colorado: USBR; 2014.

[41] Jiang H, Zhao J. Calibration of the continuous surface cap model for concrete. Finite Elements in Analysis and Design. 2015;97:1-19.

[42] CEB-FIP. CEB-FIP Model Code 1990. Comité Euro-International du Béton; 1990.

[43] Owen E. LS-Dyna Introduction to contacts. 2020.

[44] Jiang H, Chen L, Ma ZJ, Feng W. Shear Behavior of Dry Joints with Castellated Keys in Precast Concrete Segmental Bridges. Journal of Bridge Engineering. 2015;20.

[45] Zhou X, Mickleborough N, Li Z. Shear strength of joints in precast concrete segmental bridges. ACI Structural Journal. 2005;102:3-11.

[46] Stander N, Basduhar A, Roux W, Liebold K, Eggleston T, Goel T et al. LS-OPT User's Manual - A Design Optimization and Probabilistic Analysis Tool for the Engineering Analyst. Livermore, California: LSTC; 2020.

[47] Livermore Software Technilogy Corporation. LS-Dyna R11 Keyword User's Manual. Livermore, California2018.

[48] Livermore Software Technilogy Corporation. LS-OPT User's Manual. Livermore, California2020.

[49] Saouma VE. Lecture Notes in Fracture Mechanics2000.

[50] Ben Ftima M, Lemery J. Asymptotic fracture energy for nonlinear simulation of mass concrete structures. Construction and Building Materials. 2021;271.

[51] Guan J, Li Q, Wu Z, Zhao S, Dong W, Zhou S. Minimum specimen size for fracture parameters of site-casting dam concrete. Construction and Building Materials. 2015;93:973-82.

[52] Bazant ZP, Becq-Giraudon E. Estimation of Fracture Energy from Basic Characteristics of Concrete. Fracture Mechanics of Concrete Structures. Cachan, France2001.

[53] Bazant ZP, Oh BH. Crack band theory for fracture of concrete. Materials and Structures. 1983;16:155-77.

[54] Wittman FH, Roelfstra PE, Mihashi H, Huang Y-Y, Zhang x-H, Nomura N. Influence of age of loading, water-cement ratopm amd rate of loading on fracture energy of concrete. Materials and Structure. 1987;20:103-10.

737 [55] Khalilpour S, BaniAsad E, Dehestani M. A review on concrete fracture energy and effective
738 parameters. Cement and Concrete Research. 2019;120:294-321.

739 [56] CEB-FIP. Model Code 2010 - Volume 1. 2010.

740 [57] Kim J-K, Lee C-S, Park C-K, Eo S-H. The fracture characteristics of crushed limestone sand
741 concrete. Cement and Concrete Research. 1997;27:1719-29.

742 [58] Beygi MHA, Kazemi MT, Nikbin IM, Amiri JV. The effect of water to cement ratio on
743 fracture parameters and brittleness of self-compacting concrete. Materials & Design. 2013;50:267-
744 76.

745 [59] Beygi MHA, Kazemi MT, Nikbin IM, Vaseghi Amiri J, Rabbanifar S, Rahmani E. The
746 influence of coarse aggregate size and volume on the fracture behavior and brittleness of self-
747 compacting concrete. Cement and Concrete Research. 2014;66:75-90.

748 [60] Curtis DD. Estimated Shear Strength of Shear Keys and Bonded Joints in Concrete Dams.
749 31st Annual USSD Conference. San Diego, California2011. p. 295-309.

750 [61] Griffith AA. VI. The phenomena of rupture and flow in solids. Philosophical Transactions of
751 the Royal Society of London Series A, Containing Papers of a Mathematical or Physical Character.
752 1997;221:163-98.

753 [62] Bruhwiler E. Fracture of Mass Concrete Under Simulated Seismic Action. Dam Engineering.
754 1990;1:153-76.

755 [63] Bruhwiler E, Broz JJ, Saouma VE. Fracture Model Evaluation of Dam Concrete. Journal of
756 Materials in Civil Engineering. 1991;3:235-51.

757 [64] Saouma VE, Broz JJ, Bruhwiler E, Boggs HL. Effect of Aggregate and Specimen Size on
758 Fracture Properties of Dam Concrete. Journal of Materials in Civil Engineering. 1991;3.

759 [65] Li Q, Guan J, Wu Z, Dong W, Zhou S. Fracture Behavior of Site-Casting Dam Concrete. ACI
760 Materials Journal. 2015;112.

761 [66] Bakour A, Ben Ftima M. Experimental investigations on the asymptotic fracture energy for
762 large mass concrete specimens using wedge splitting test. Construction and Building Materials.
763 2021;279.

764
765

Appendix Table A.1 – Experimental Data on G_F

Source	Specimen	fc (MPa)	ft (MPa)	d_a (mm)	h_2 (mm)	h_2/d_a	E (GPa)	w/c	GF (N/m)
Bruhwiler [62]	Arch Dam A	48*	2.4	80	-	-	36	0.5*	230.0
	Arch Dam B	46*	2.3	120	-	-	27	0.5*	310.0
	Arch Dam C	40*	2	120	-	-	29	0.5*	270.0
	Structural Concrete	68*	3.4	32	-	-	36	0.5*	140.0
Bruhwiler et al. [63]	Medium	45.4*	2.27	38	610	16.1	17.2	0.5*	222.0
	Medium	41*	2.05	76	610	8.0	17.3	0.5*	226.0
	Large	45.4*	2.27	38	1081	28.5	16.7	0.5*	259.0
	Large	41*	2.05	76	1081	14.2	14.1	0.5*	236.0
Saouma et al. [64]	Small	24.8	2.67	38	200	5.3	16.9	0.55	240.0
	Medium	36.6	3.96	38	610	16.1	23.2	0.55	227.0
	Large	18.9	2.41	76	1070	14.1	16.5	0.55	230.0
Li et al. [65]	D800-28	26.64	2.7	150	480	3.2	23	0.41	520.0
	D800-90	30.5	3.21	150	480	3.2	25	0.41	600.2
	D800-180	30.75	3.24	150	480	3.2	26.2	0.41	631.8
	D1000-180	30.75	3.24	150	600	4.0	26.2	0.41	850.0
	D1200-180	30.75	3.24	150	720	4.8	26.2	0.41	579.9
Guan et al. [51]	FG800	29.37	3.04	150	480	3.2	26.12	0.41	504.9
	FG1000	29.37	3.04	150	600	4.0	26.12	0.41	567.2
	FG1200	29.37	3.04	150	720	4.8	26.12	0.41	643.8
	FG1500	29.37	3.04	150	900	6.0	26.12	0.41	754.6
	FG2250	29.37	3.04	150	1350	9.0	26.12	0.41	759.7
Ben Ftima and Lemery [50]	A38	20.3	2	38	179	4.7	25	0.58	449.0
	A76	25.4	2	76	405	5.3	25	0.58	646.0
	B76 (with NaOH)	23.7	2	76	423	5.6	25	0.58	589.0
Bakour and Ben Ftima [66]	WS-700-2 Exp.	34.8	2.088*	100	528	5.3	29.4	0.55	386.0
	WS-700-5 Exp.	34.8	2.088*	100	330	3.3	29.4	0.55	288.0
	WS-700-2 DFPZ	34.8	2.088*	100	528	5.3	29.4	0.55	459.0
	WS-700-2 SBEM	34.8	2.088*	100	528	5.3	29.4	0.55	550.0
	WS-2440-05 C1	34.8	2.088*	100	1170	11.7	29.4	0.55	335.0
	WS-2440-05 C2	34.8	2.088*	100	1170	11.7	29.4	0.55	458.0

*Estimated values that are not specified in the source

Note: values of h_2 are not reported in Bruhwiler [62]